The Influence of Vertical Wind Shear on the Evolution of Mountain-Wave Momentum Flux

DALE R. DURRAN AND MAXIMO Q. MENCHACA

Department of Atmospheric Sciences, University of Washington, Seattle, Washington

(Manuscript received 2 August 2018, in final form 1 December 2018)

ABSTRACT

The influence of vertical shear on the evolution of mountain-wave momentum fluxes in time-varying cross-mountain flows is investigated by numerical simulation and analyzed using ray tracing and the WKB approximation. The previously documented tendency of momentum fluxes to be strongest during periods of large-scale cross-mountain flow acceleration can be eliminated when the cross-mountain wind increases strongly with height. In particular, the wave packet accumulation mechanism responsible for the enhancement of the momentum flux during periods of cross-mountain flow acceleration is eliminated by the tendency of the vertical group velocity to increase with height in a mean flow with strong forward shear, thereby promoting vertical separation rather than concentration of vertically propagating wave packets.

1. Introduction

Gravity waves, which are frequently generated when air flows over a ridge, are associated with vertical fluxes of horizontal momentum. A decelerative force is exerted on the cross-mountain flow in regions of vertical momentum flux divergence. As an example, mountain waves frequently break down in the lower stratosphere, where the momentum-flux divergence associated with this breaking produces "gravity wave drag." The important influence of gravity wave drag on the large-scale flow over mountains has long been recognized (Sawyer 1959; Lilly 1972; Smith 1979), and this effect is parameterized in all coarse-resolution weather and climate models [see Kim et al. (2003) for a review].

The accurate parameterization of gravity wave drag is difficult because, among other things, its magnitude can be a sensitive function of nonlinear processes (Durran 1992) and boundary layer structure (Smith 2007). Another potential source of difficulty was suggested by Chen et al. (2005, hereafter CDH05), who noted that the momentum flux can depend on the temporal variations in the cross-mountain flow. They simulated mountain waves above an isolated ridge generated by the passage of a large-scale barotropic jet in which N and U were constant with height at any given x, y, and t. Even in cases where the cross-mountain flow varied on slow multiday time scales, CDH05 found that the mountain-wave momentum fluxes were significantly enhanced during the period of large-scale flow acceleration and diminished during deceleration. Ray tracing and WKB analysis showed that the enhancement of the momentum flux during the accelerating phase was produced by the tendency of wave packets launched when the flow was stronger to have higher vertical group velocities than packets launched when the winds were slower. As a consequence of their higher group velocities, those packets launched later overtook the packets launched earlier, thereby producing an accumulation of wave packets and intense momentum fluxes several kilometers above the surface.

To examine nonsteady mountain waves and momentum fluxes in a more realistic but still idealized environment, Menchaca and Durran (2017, hereafter MD17) conducted simulations of a midlatitude cyclone growing in a baroclinically unstable flow encountering an isolated 3D ridge. The mountain-wave momentum fluxes develop differently in these new simulations: the strongest fluxes occur near the surface after the passage of the strongest large-scale cross-mountain winds. The key factor producing the difference between the momentum fluxes in the current simulation and those in CDH05 is the vertical shear in the large-scale cross-mountain wind. In the following we document this

Corresponding author: Dale R. Durran, drdee@uw.edu

DOI: 10.1175/JAS-D-18-0231.1

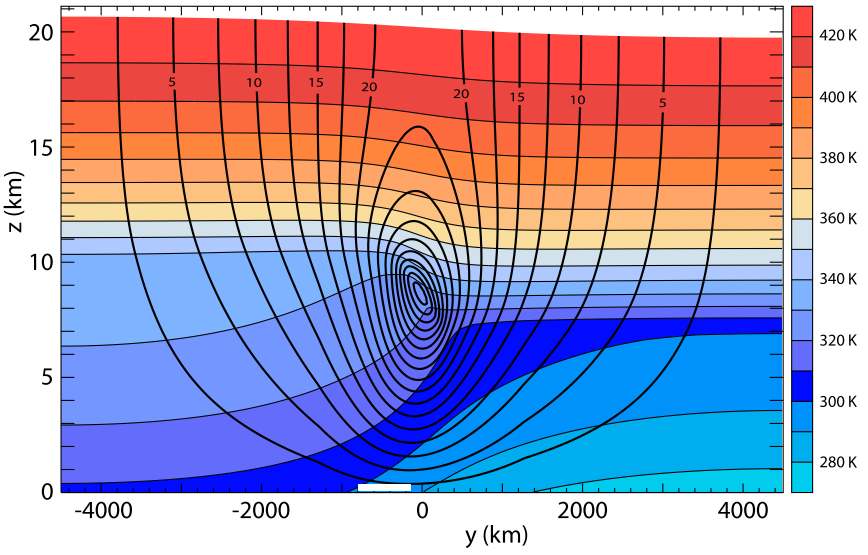

FIG. 1. North–south cross section through the background shear flow: θ (color fill at 10-K intervals) and zonal velocity (contoured in black at 2.5 m s^{-1} intervals). The white bar extending from $-800 \le y \le -160$ km shows the north–south extent of the ridge. Data are not plotted in the wave-absorbing layer.

difference and analyze the role of mean shear using ray tracing and WKB theory.

A brief overview of the numerical simulations is presented in section 2. The vertical distribution of the mountain-wave momentum flux triggered by the baroclinically unstable jet is discussed in section 3. A ray-tracing and WKB analysis of the influence of the vertical shear on the accumulation of wave packets above the mountain during periods of mean-flow acceleration is given in section 4. Section 5 contains the conclusions.

2. Simulation details and large-scale flow

The large-scale flow and the initiation of the cyclone are described in MD17, along with the shape of the isolated ridge, whose approximate x and y extents are 80 and 640 km, respectively. Our focus is on the simulation with the lower 500-m-high ridge for which the waves do not break and a quasi-linear analysis is appropriate. This simulation uses an outer grid on which $\Delta x = \Delta y = 15$ km and an inner nest where $\Delta x = \Delta y = 5$ km. The vertical domain extends to approximately[1] 26.5 km, with 95 vertical levels over which Δz increases from 30 m near the surface to 400 m near the base of the damping layer. A 6-km-deep Rayleigh damping layer occupies the region $20.5 \le z \le 26.5$ km to absorb gravity waves. As discussed in MD17, the mountain waves in this simulation are sensitive to the geometry of the damping layer, and this configuration keeps the overall computational burden tractable while ensuring the damping-layer-induced sensitivities are modest.

Figure 1 is a y–z cross section showing isotachs of the westerly wind component and isentropes of potential temperature in the initial unperturbed baroclinically unstable shear flow. The north–south position of the mountain is shown by the white bar above the y axis, which is just south of the core of the jet. As discussed in MD17, a cyclone is triggered by an isolated PV perturbation; its evolution between 2.5 and 7.5 days is illustrated by the surface isobars and θ fields plotted in Fig. 2. Note that the cold front arrives at the ridge at around 4.5 days. The full extent of the nested mesh is shown by the dashed red box in Fig. 2a.

The mountain waves that develop during and after the interaction of the cold front with the mountain are shown in Fig. 3 by contours of the vertical velocities and isentropes in an x–z vertical cross section through the center of the mountain at 4.5, 5.5, 6.5, and 7.5 days (Fig. 3a–d, respectively). The waves are clearly strongest at 6.5 days, with vertical-velocity extrema of roughly ± 1.5 m s^{-1}, but even at this time there is no wave breaking. There are nontrivial north–south variations in the structure of these waves, which are illustrated in Figs. 5 and 6–9a,b of MD17, but the temporal variation in the spatially averaged strength of the wave response is well illustrated in Fig. 3.

[1] Because of the WRF Model's vertical coordinate, the height of the model top varies slightly in space and time.

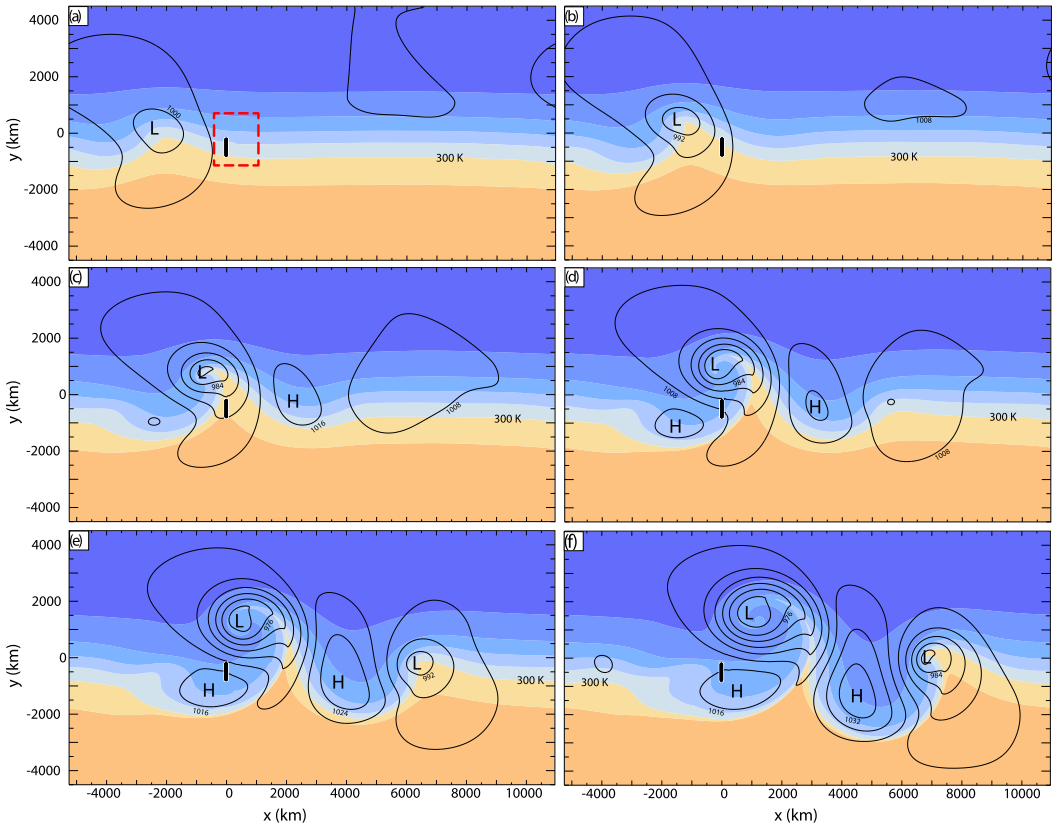

FIG. 2. Surface isobars (black lines at 8-hPa intervals) and surface θ (color fill at 5-K intervals) for the developing cyclone at (a) 2.5, (b) 3.5, (c) 4.5, (d) 5.5, (e) 6.5, and (f) 7.5 days. The mountain is depicted by the black vertical bar at $x = 0$ km in all panels. The nested grid is shown by the red dashed lines in (a). Lows and highs are labeled by "L" and "H", respectively.

3. Vertical momentum flux distribution

The terrain-induced velocities (u', v') will be evaluated as the difference between the fields in a pair of simulations conducted with and without the mountain. The vertical flux of the terrain-induced x-component momentum within the subdomain $[x_1, x_2] \times [y_1, y_2]$ is computed as

$$M'(z,t) = \int_{x_1}^{x_2}\int_{y_1}^{y_2} \rho u' w' \, dy \, dx; \qquad (1)$$

here $\overline{\rho}(z)$ is background density at elevation z. In the subsequent analysis, $(x_1, x_2) = (-372, 1145)$ km and $(y_1, y_2) = (-1128, 172)$ km, which gives the maximum sized box having the terrain centered in the north–south direction that fits within the fine-nest subdomain. A mountain-induced pressure drag may be computed as

$$P'(t) = -\int_{x_1}^{x_2}\int_{y_1}^{y_2} p'[x, y, h(x,y), t] \frac{\partial h}{\partial x} \, dy \, dx, \qquad (2)$$

where the terrain-induced pressure perturbation p' is the difference in pressure between pairs of simulations conducted with and without the mountain. At heights z_l below the top of the mountain, the mountain-induced pressure drag generated by the portion of the ridge extending above z_l is added to the momentum fluxes computed at the same level in the free air.[2]

The horizontally integrated momentum flux M' triggered by the interaction of the baroclinically unstable jet with the 500-m-high ridge is plotted as a function of time and height in Fig. 4. Prior to day 5.5, which is approximately the time of maximum low-level cross-mountain flow, and after day 6.8, M' is almost constant with height. Between 5.5 and 6.8 days the momentum flux is strongest near the surface and decays with height up to roughly $z = 5$ km. This low-level vertical momentum flux divergence is not due to wave breaking, which does not occur over the comparatively low 500-m-high mountain. Vertical momentum flux gradients were also evident in the idealized

[2] The sum of these two quantities is the total vertical momentum flux through the bottom of a volume bounded by $z = z_l$ and the penetrating mountain top.

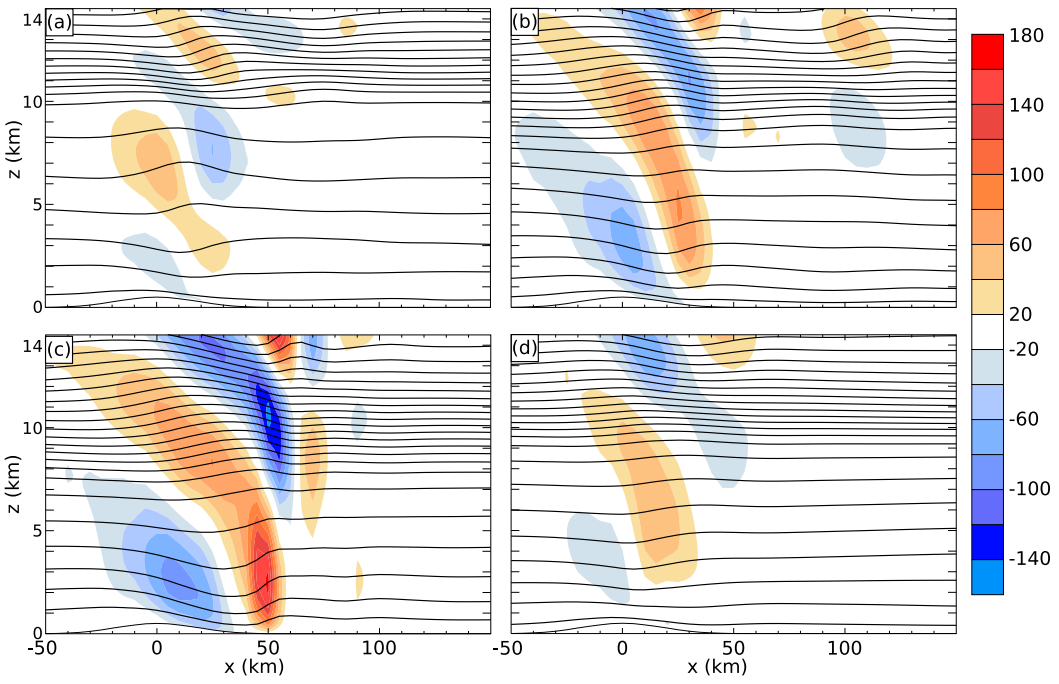

FIG. 3. East–west vertical cross sections of w (color fill at 20 cm s^{-1} intervals) and θ (black lines at 5-K intervals) across the centerline of the mountain at (a) 4.5, (b) 5.5, (c) 6.5, and (d) 7.5 days.

simulations of time-dependent flow over an isolated ridge in CDH05, but the pattern in that case (their Fig. 4a) was very different, with maximum momentum fluxes aloft before the time of maximum wind.

Since there is no wave breaking, the wave packet accumulation mechanism responsible for the enhancement aloft during the period of flow acceleration in CDH05 might be expected to produce a similar response in the current simulation. Why is the momentum flux distribution in Fig. 4 different? The key difference is the vertical shear in the large-scale cross-mountain flow, which was zero in CDH05, but, at 6.5 days in the present simulation, is roughly 20 m s^{-1} between the surface and 5 km.

4. The influence of vertical shear

To evaluate the influence of the vertical shear in the simplest context, consider a 2D horizontally homogeneous large-scale flow in an (x, z) plane over a mountain. In a WKB framework, the dispersion relation for hydrostatic gravity waves in this basic state is

$$\omega(k,m,z,t) = U(z,t)k - N\frac{k}{m}, \tag{3}$$

where ω is the frequency, and k and m are the horizontal and vertical wavenumbers, respectively; N will be assumed constant, $U(z, t)$ is assumed to be positive, and the minus sign is chosen because our focus is waves that propagate upstream relative to the flow. The vertical group velocity is

$$c_{g_z} = \frac{\partial\omega}{\partial m} = N\frac{k}{m^2}. \tag{4}$$

Ray tracing theory (Lighthill 1978, section 4.5) applied to (3) gives

$$\frac{D_g k}{Dt} = -\frac{\partial\omega}{\partial x} = 0 \tag{5}$$

and

$$\frac{D_g m}{Dt} = -\frac{\partial\omega}{\partial z} = -k\frac{\partial U}{\partial z}, \tag{6}$$

where

$$\frac{D_g}{Dt} = \frac{\partial}{\partial t} + c_{g_x}\frac{\partial}{\partial x} + c_{g_z}\frac{\partial}{\partial z} \tag{7}$$

is the total derivative following a ray path. Note that (6) implies that m remains constant along a ray path when there is no vertical shear in the background wind. From (4)–(6), the change in the vertical group velocity along a ray path is, therefore,

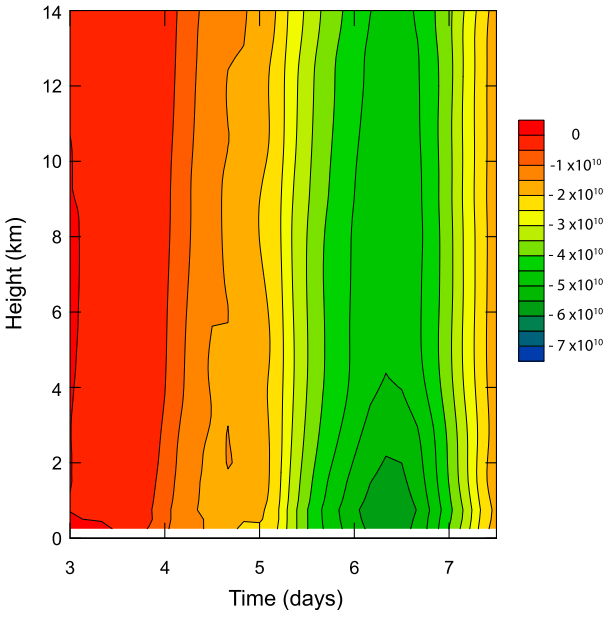

FIG. 4. The momentum flux M' (contour intervals of 0.5×10^{10} N) generated by the baroclinically unstable jet passing over a 500-m-high mountain as a function of z and t. At heights z_l below the top of the mountain, the pressure drag due to the portion of the ridge extending above z_l is added to the fluxes computed at the same level in the free air (see text).

$$\frac{D_g c_{g_z}}{Dt} = Nk\frac{D_g}{Dt}\left(\frac{1}{m^2}\right) = 2\frac{Nk}{m^3}\frac{\partial\omega}{\partial z} = 2\frac{Nk^2}{m^3}\frac{\partial U}{\partial z}. \tag{8}$$

If there is no vertical wind shear, then the vertical group velocity remains constant as the packet propagates upward from the surface.

As was justified by the results in CDH05, the mountain waves are assumed to be in approximately steady at the time t_l when a wave packet is first launched; then (3) implies $U(0, t_l)k = Nk/m$; solving this for m and substituting in (4), the vertical group velocity at the surface at time t_l is[3]

$$c_{g_z}(0, t_l) = U(0, t_l)^2\frac{k}{N}. \tag{9}$$

When $U(0, t_l)$ increases with time, (9) implies that packets launched at later times have larger vertical group velocities and will tend to overtake those launched earlier (although they do not accumulate at the same horizontal location, as illustrated in Fig. 5b in CDH05). But if U increases with height, (8) implies that c_{g_z} will increase along the ray path,[4] and there will be a tendency for wave packets to disperse in the vertical. The wave packet accumulation found by CDH05 can, therefore, be avoided if the rate at which c_{g_z} increases along a ray path owing to vertical shear is greater than the rate at which c_{g_z} increases owing to the acceleration of the cross-mountain flow, that is, if

$$\frac{\partial c_{g_z}}{\partial t} < \frac{D_g c_{g_z}}{Dt}. \tag{10}$$

The condition (10) can easily be evaluated at the surface. Differentiating (9) with respect to time and substituting the vertical wavenumber for steady waves $m = N/U(0, t_l)$ in (8) shows that wave packets will not accumulate in the vertical if

$$\frac{\partial U(0,t)}{\partial t} < \frac{U(0,t)^2 k}{N}\frac{\partial U(0,t)}{\partial z} \tag{11}$$

or, alternatively, if

$$\frac{\partial U(0,t)}{\partial t} < c_{g_z}(0, t_l)\frac{\partial U(0,t)}{\partial z}. \tag{12}$$

To appreciate the influence of vertical shear in a simple numerical example, consider a two-dimensional (x–z) horizontally uniform large-scale flow that accelerates from rest and varies sinusoidally with time over a period $\tau = 50$ h, such that

$$U_{2d}(z,t) = u(z)\left[1 - \cos\left(\frac{2\pi t}{\tau}\right)\right], \tag{13}$$

where

$$u(z) = \begin{cases} 10\,\mathrm{m\,s^{-1}} + \alpha z & z \le 10\,\mathrm{km} \\ 10\,\mathrm{m\,s^{-1}} + \alpha \times 10\,\mathrm{km} & z > 10\,\mathrm{km} \end{cases}. \tag{14}$$

This flow starts from rest, accelerates to a maximum speed of $2u(z)$ at $t = \tau/2$, and then decelerates back to zero. Three cases, $\alpha = 0$, 5×10^{-4}, and $10 \times 10^{-4}\,\mathrm{s^{-1}}$, will be examined through numerical simulation using the model in a 2D x–z configuration.

The mountain profile is taken parallel to the x axis along the center line of the 3D mountain [i.e., is given by Eq. (1) in MD17 evaluated at $y = 0$] except that its maximum height is 250 m to make the dynamics more linear. Consistent with the preceding WKB analysis, the Coriolis force is set to zero. The numerical parameters are identical to those in the 3D mountain simulation except that the Rayleigh damping layer is now 14 km thick (starting at $z = 17$ km); the functional form of the damping profile is given by Eq. (2) in MD17, with $\beta_{max} = 0.0025$. The deeper damping layer is accommodated by raising the top of the domain to

[3] Consistent with the linear analysis, here we take $z = 0$ as the elevation of the surface.

[4] The vertical wavenumber is positive because $m = N/U(0, t_l)$ when the packet is launched.

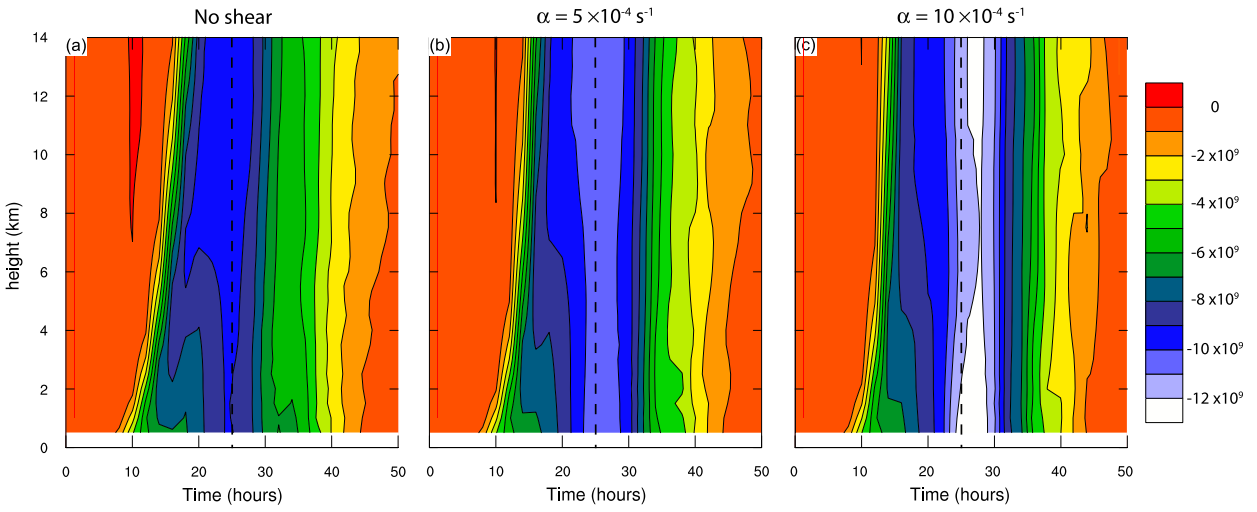

FIG. 5. Momentum fluxes M'_{2d} (contour intervals of $10^9\,\mathrm{N\,m^{-1}}$) in a horizontally uniform nonsteady large-scale flow impinging on a 250-m-high mountain as a function of height and time for background flows with (a) no shear, and maximum 0–10-km shear of (b) 10 and (c) $20\,\mathrm{m\,s^{-1}}$. Vertical dashed lines are plotted for reference at the time of maximum large-scale cross-mountain wind.

31 km. The first 80 vertical levels are initialized with values of ϕ, θ, p, and ρ identical to those in the 3D simulation at 4.5 days, 200 km upstream of the mountain, and 100 km south of its centerline [i.e., at $(x, y) = (-200, -580)$ km]. This basic state is then extended upward across another 25 levels using constant values of Δz and N equal to their averages over the top five levels of the original domain.

The maximum acceleration of the large-scale flow, as well as the greatest potential for wave packet accumulation, occurs at 12.5 h ($t = \tau/4$). Taking 80 km as a representative wavelength for the mountain profile, $N = 0.01\,\mathrm{s^{-1}}$, and using (14), both sides of (11) will be equal when $\alpha = 4.45 \times 10^{-4}\,\mathrm{s^{-1}}$. Having chosen a nonsinusoidal mountain shape and a thermodynamic profile to closely match the upstream conditions in the baroclinic flow, rather than the constant N assumed in the WKB analysis, we can only expect (11) to give approximate quantitative guidance. We therefore anticipate the wave packet accumulation mechanism will be largely neutralized in the case where $\alpha = 0.5 \times 10^{-4}\,\mathrm{s^{-1}}$. Wave packet accumulation might be expected to be replaced by an increasing vertical separation of the packets in the stronger shear case, $\alpha = 10^{-4}\,\mathrm{s^{-1}}$.

Horizontally averaged momentum fluxes

$$M'_{2d}(z,t) = \int_{x_1}^{x_2} \rho(u - U_{2d})w'\,dx \qquad (15)$$

are plotted for all three cases as a function of time and height in Fig. 5. The pattern of M'_{2d} in the no shear case (Fig. 5a) is very similar to that in Fig. 4c of CDH05, instead of being constant with height and symmetric in magnitude about the time of maximum cross-mountain flow, stronger momentum fluxes develop aloft during the period of mean-flow acceleration.[5] Most of the momentum flux enhancement during the acceleration phase disappears in the case with moderate shear (Fig. 5b), and the maximum momentum fluxes occur just slightly after the time of maximum wind. In the most strongly sheared case (Fig. 5c), for which the magnitude of the 0–10-km shear rises to $20\,\mathrm{m\,s^{-1}}$ at the time of maximum wind, the maximum momentum fluxes at all levels occur after the time of maximum cross-mountain wind, and at $t = 27$ h there is a slight decrease in M'_{2d} between the surface and the 8-km level reminiscent of the vertical gradient at $t = 6.3$ days in Fig. 4.

In summary, as the vertical shear is increased in the 2D simulations shown in Fig. 5, the time-height distribution of M'_{2d} shifts from a pattern similar to that generated by the barotropic jet in CDH05 toward the distribution of M' generated by the complex baroclinic system in Fig. 4. Noting that the shear near the time of maximum cross-mountain wind in the baroclinic system is similar to that in the strongest 2D case, we conclude that the lack of enhanced momentum fluxes during the period of cross-mountain flow acceleration and the decrease in M' with height at $t = 6.3$ days in Fig. 4 are most likely produced by the vertical divergence of wave packets in strongly sheared flow.

[5] Differences between this case and that in CDH05 arise because in that case the flow is not horizontally homogeneous and N is constant with height (no stratosphere).

Another factor that might influence the vertical gradient of M' is acceleration by the Coriolis force, which combines with the vertical momentum flux to balance the surface pressure drag in steady linear flow P'_f such that

$$P'_f = \int_0^{2\pi/k} \rho(u' - f\eta')w'\,dx, \tag{16}$$

where η' is the displacement parallel to the y coordinate produced by the perturbation y-component velocities, the topography is assumed sinusoidal with wavenumber k, and f the Coriolis parameter (Jones 1967; Bretherton 1969). As discussed in Menchaca and Durran (2018), in this simulation Coriolis effects are sufficiently small that P' provides a good estimate of M', implying that the Rossby number associated with the environmental cross-mountain flow is large enough to make the $f\eta'w'$ term in (16) insignificant. Furthermore, the $f\eta'w'$ term was not important in the simulations in CDH05 (see their Fig. 4c), which is a case for which the Rossby number, computed using the cross-mountain length scale, is less than half that for the case in Fig. 4, and of course $f = 0$ for the simulations shown in Fig. 5. It therefore appears that the decrease with height in the low-level momentum fluxes in Fig. 4 is indeed produced by the tendency of vertical shear to disperse vertically propagating wave packets.

5. Conclusions

We numerically simulated the mountain waves generated as an idealized cyclone growing in a baroclinically unstable flow passes over an isolated 3D 500-m-high ridge. This experimental design avoids artificial start-up transients in the mountain-wave field, thereby facilitating the analysis of the temporal evolution of the momentum fluxes associated with these waves. The mountain height is low enough that there is no wave breaking during the simulation. The momentum fluxes remain relatively constant with height until about the time when the large-scale cross-mountain winds reach their maximum speed. The strongest vertical momentum fluxes occur after the time of maximum winds, roughly between 5.5 and 7 days, when the momentum fluxes decrease with height between the surface and 5 km.

These results differ from the behavior documented in CDH05 for a barotropic jet crossing a similar isolated ridge in which wave packets launched later during the accelerating phase of the large-scale flow accumulate aloft, thereby maximizing the momentum flux during the period of flow acceleration and creating a layer at low levels throughout which the momentum fluxes increase with height. Ray tracing and WKB analysis suggest that the vertical momentum flux profile evolves differently in the current simulation because the vertical shear in the baroclinic jet prevents the accumulation of wave packets aloft. This analysis is supported by additional 2D simulations of waves in shear flows that vary periodically with time. When the vertical shear in the environmental wind is zero, the momentum flux evolution in the 2D simulation was similar to that in CDH05. On the other hand, in the case with the strongest shear, the momentum flux evolution was similar to that generated by the isolated ridge in the baroclinically unstable shear flow.

The weaker sensitivity of the momentum flux to the past history of the flow in large-scale environments where the cross-mountain winds increase with height is good news for those attempting to improve gravity wave-drag parameterizations over mountains exposed to the midlatitude westerlies. Nevertheless, flow transience can still exert an important influence on the momentum flux in such flows by setting the magnitude of the flux. The importance of transience in regulating the momentum flux (and the surface pressure drag) was demonstrated in Menchaca and Durran (2018) by comparing the simulation with the evolving baroclinic jet with other 3D simulations in which the mountain waves were forced by the same isolated 500-m-high ridge in steady large-scale flows representative of the instantaneous near-mountain environment at four successive times in the evolving flow. At 6.5 days, when M' reaches its extremum, and at 7.5 days, the evolving baroclinic jet generated momentum fluxes that were roughly 50% larger than those for simulations with the corresponding steady large-scale flows. On the other hand, there is some evidence that a precise representation of the mountain-wave dynamics can be avoided in gravity wave drag parameterizations on sufficiently large scales. In particular Smith and Kruse (2018) have had success estimating surface pressure drags over the entire south Island of New Zealand using a very simple linear mountain-wave model and a more sophisticated representation of the effective smoothness of the terrain under different wind speeds.

Acknowledgments. This research is funded by NSF Grant AGS-1545927. Author Menchaca was also supported by a National Science Foundation Graduate Research Fellowship. Three anonymous reviewers provided very helpful comments. We gratefully acknowledge high-performance computing support from Yellowstone (ark:/85065/d7wd3xhc) provided by NCAR's Computational and Information Systems Laboratory, sponsored by the National Science Foundation.

REFERENCES

Bretherton, F., 1969: Momentum transport by gravity waves. *Quart. J. Roy. Meteor. Soc.*, **95**, 213–243, https://doi.org/10.1002/qj.49709540402.

Chen, C.-C., D. R. Durran, and G. Hakim, 2005: Mountain-wave momentum flux in an evolving synoptic-scale flow. *J. Atmos. Sci.*, **62**, 3213–3231, https://doi.org/10.1175/JAS3543.1.

Durran, D. R., 1992: Two-layer solutions to Long's equation for vertically propagating mountain waves: How good is linear theory? *Quart. J. Roy. Meteor. Soc.*, **118**, 415–433, https://doi.org/10.1002/qj.49711850502.

Jones, W. L., 1967: Propagation of internal gravity waves in fluids with shear flow and rotation. *J. Fluid Mech.*, **30**, 439–448, https://doi.org/10.1017/S0022112067001521.

Kim, Y.-J., S. D. Eckermann, and H.-Y. Chun, 2003: An overview of the past, present and future of gravity-wave drag parametrization for numerical climate and weather prediction models. *Atmos.–Ocean*, **41**, 65–98, https://doi.org/10.3137/ao.410105.

Lighthill, J., 1978: *Waves in Fluids.* Cambridge University Press, 504 pp.

Lilly, D. K., 1972: Wave momentum flux—A GARP problem. *Bull. Amer. Meteor. Soc.*, **53**, 17–23, https://doi.org/10.1175/1520-0477-53.1.17.

Menchaca, M. Q., and D. R. Durran, 2017: Mountain waves, downslope winds, and low-level blocking forced by a midlatitude cyclone encountering an isolated ridge. *J. Atmos. Sci.*, **74**, 617–639, https://doi.org/10.1175/JAS-D-16-0092.1.

——, and ——, 2018: The impact of mountain waves on an idealized baroclinically unstable large-scale flow. *J. Atmos. Sci.*, **75**, 3285–3302, https://doi.org/10.1175/JAS-D-17-0396.1.

Sawyer, J. S., 1959: The introduction of the effects of topography into methods of numerical forecasting. *Quart. J. Roy. Meteor. Soc.*, **85**, 31–43, https://doi.org/10.1002/qj.49708536304.

Smith, R. B., 1979: The influence of the mountains on the atmosphere. *Advances in Geophysics*, Vol. 21, Academic Press, 87–230.

——, 2007: Interacting mountain waves and boundary layers. *J. Atmos. Sci.*, **64**, 594–607, https://doi.org/10.1175/JAS3836.1.

——, and C. G. Kruse, 2018: A gravity wave drag matrix for complex terrain. *J. Atmos. Sci.*, **75**, 2599–2613, https://doi.org/10.1175/JAS-D-17-0380.1.